A Nanoscale Model for Characterizing the Complex Pore Structure of Biochars

Kyriacos Zygourakis and Hao Sun
Dept. of Chemical and Biomolecular Engineering, Rice University, Houston, TX 77005

Pauline Markenscoff
Dept. of Electrical and Computer Engineering, University of Houston, TX 77204

DOI 10.1002/aic.14134
Published online June 28, 2013 in Wiley Online Library (wileyonlinelibrary.com)

The development of a novel nanoscale model that can accurately describe the reactivity of solids consisting of multiple components and having ordered and random pores is presented. Domains of multiple solid phases are distributed on a computational grid to simulate reactants with different specific reactivities and dispersions. Sub-nanometer slit pores and larger cylindrical pores with given size distributions are also distributed on the grid in regular and random arrangements respectively. The generated solids are then eroded using rules that simulate a gas-solid, non-catalytic reaction occurring in the kinetic control regime. A parametric study is first carried out to demonstrate how key pore structural parameters affect the reactivity patterns. Model predictions are found to be in excellent agreement with experimental thermogravimetric data for the combustion of biochars, both when the slit and random cylindrical pores are fully accessible to the reactant and when diffusional limitations appear in the smaller slit pores. © 2013 American Institute of Chemical Engineers *AIChE J*, 59: 3412-3420, 2013
Keywords: micropore structure, diffusion-reaction, discrete mathematical model, combustion, biochar

Introduction

In a series of landmark papers, Neal Amundson with several of his students laid the foundation for understanding the mechanisms that govern the combustion of porous carbonaceous materials. The earlier models considered the problem of diffusion and reaction in the boundary layer surrounding a single carbon particle, using reaction rate expressions that lumped the kinetics and intraparticle diffusional resistance onto the particle's external surface.[1–8] Although these lumped models provided for the first time an accurate description of the combustion process for some operating conditions, they did not consider the dynamic interplay between intraparticle diffusion and reaction. As the carbon is consumed, the pore structure changes affecting the relative magnitudes of transport and reaction rates.

Several investigators tackled this problem by focusing on the development of random pore models that could describe how the temporal evolution of the internal pore structure affects the transient combustion rates.[9–14] In general, these models described the internal pore structure of a char particle as a network of randomly overlapping objects (pores or grains) with different geometries. Two competing processes modulate the temporal evolution of such pore structures as reaction proceeds: pore growth and coalescence of neighboring pores as the walls separating them are consumed by the reaction. Pore enlargement is prominent at low conversions and may result in increases of the surface area and the observed reaction rate. As pores continue to grow, however, they coalesce with adjacent enlarging pores, causing the pore surface area and combustion rate to decrease. Thus, the reaction rate vs. conversion curves may exhibit maxima or may decrease monotonically with conversion when pore coalescence dominates from the early stages of reaction. The predicted evolution patterns of internal pore surface area can then be compared to experimental gasification data to validate the models.[11,12,15–18]

The importance of this dynamic interplay between intraparticle mass transport and reaction for combustion at high temperatures was demonstrated in the seminal papers of Sotirchos and Amundson.[19–23] These studies quantified the significant effects of intraparticle mass transport, different patterns of internal surface area evolution, and intraparticle thermal gradients on the pseudosteady-state and transient combustion rates. To estimate the intraparticle diffusional resistance, Sotirchos and Amundson introduced model simplifications that neglected diffusion in micropores and only considered diffusional resistances in the macropores. Macropore diffusional resistance was lumped into a parameter representing the average macropore size. Their pseudosteady-state analysis revealed an ambient temperature range where multiple solution loci existed for the particle internal temperature. They also concluded that the inclusion of intraparticle thermal gradients significantly affected the solution structure by expanding the multiplicity region and shifting it to lower ambient temperatures.

To account for the diffusional resistance in micropores, Sotirchos and Burganos[24] further refined the model by incorporating the random pore model of Gavalas[25] into their

Correspondence concerning this article should be addressed to K. Zygourakis at kyzy@rice.edu.

analysis. The diffusion model of Feng and Stewart[26] was then used to lump the diffusional resistance in macro- and micropores into a single effective diffusional coefficient. This model effectively demonstrated that the increasing diffusional resistance shrank the multiplicity region and shifted it toward higher ambient temperatures, thus making it more difficult for ignitions to occur.

This class of random pore models[27,28] did not explicitly account for the presence of an extensive network of large spherical cavities observed in chars derived from pyrolyzing plastic coals.[29,30] Cai and Zygourakis addressed this issue by developing a multiscale model that visualized the pore structure as an interconnected network of randomly dispersed large cavities separated by walls consisting of microporous grains containing carbon and ash.[31] Their analysis concluded that the porosity and surface area associated with large cavities would drastically affect the reactivity and ignition behavior of char particles in the regime of pore diffusional limitations. This effect diminishes when combustion takes place in the regimes of kinetic or external mass-transfer control.

However, the random pore models described in these studies could not always provide an accurate description of the temporal evolution of pore surface areas and, consequently, of the combustion rates of solid reactants. To overcome this limitation, Sandmann and Zygourakis[32,33] developed a new class of discrete models that could simulate the combustion of solids with arbitrary spatial and size distributions of pores. Results from simulations with the discrete models agreed very well with the theoretical predictions of continuous random pore (or grain) models.[9,14,25,27,28] More importantly, however, the discrete models allowed for easy simulation of the reaction of solids with pore structures characterized by completely or partially ordered pores. In the latter case, the solids had two pore subpopulations: one with pores that are randomly distributed in space and a second one with pores that followed a regular spatial arrangement. We must note here that partially ordered pore structures have been experimentally discovered in heat-treated carbonaceous materials[34–36] and are consistent with mechanisms involving the appearance of a liquid crystalline phase (carbonaceous mesophase) during the pyrolysis stage.[37] According to these mechanisms, liquid crystalline regions are formed due to a partial ordering of planar fused-ring macromolecules produced by the aromatic condensation reactions occurring during pyrolysis.

Simulations with partially ordered pore structures generated reactivity patterns that exhibited maxima at low conversions and/or inflection points, features that were observed experimentally but could not be simulated with random pore (or grain) models.[33] Discrete simulations with completely ordered pore structures also produced complex surface area evolution patterns exhibiting inflection points, sharp maxima, and large constant area regions or initial steep decreases in surface area.[32]

A new approach for probing the pore structure of solid reactants

These earlier studies built a theoretical framework that can facilitate the characterization of the complex pore structure of biochars, an important class of carbonaceous materials that can be used for carbon sequestration and soil amendment. Biochars have complex pore structures consisting of multiple interconnected networks of micropores, mesopores, and macropores that span multiple length scales: from subnanometer micropores to macropores with sizes of the order of 10 microns. Such pore structures cannot be characterized by a single analytical technique. Instead, a combination of time-consuming analytical techniques must be used to bridge the vastly different length scales: adsorption of multiple gases (such as nitrogen, carbon dioxide, and water) for the micropores, mercury porosimetry for the mesopores, and sectioning with optical microscopy and three-dimensional (3-D) reconstruction techniques for the macropores.

The studies discussed in the previous section show how experimental reactivity data can be used to probe and characterize the multiscale pore structures of solid reactants. At low temperatures, combustion proceeds in the regime of kinetic control and the entire surface area attributed to micropores (or even the submicropores) is completely accessible to the reactant. As the temperature rises, the reaction regimes shifts to diffusion control and strong diffusional resistances start appearing first in the micropores, then in the mesopores, and, subsequently, in the macropores. As a result, larger and larger fractions of the micropore and mesopore structure will become inaccessible to oxygen as the temperature is raised. Finally, at sufficiently high temperatures, combustion will take place only on the micropore and mesopore "mouths" where they open up into the large macropore cavities identified in scanning electron microscopy (SEM) or optical microscopy images.

The different experimental reactivity patterns obtained as we move from the kinetic control regime to that of strong diffusional limitations reveal a wealth of information about the size, shape, and spatial arrangement of the pores participating in the reaction.[38] To quantify this information, however, we need a theoretical model that can accurately describe the pore structure of solid reactants and its evolution in the various reaction regimes. Once such a model is available, we will be able to estimate any pore structure parameters that cannot be determined by direct analytical measurements by matching model predictions to experimental reactivity data.

We present here the development of a nanoscale model that can accurately describe the reactivity of solids consisting of multiple components and having a mixture of ordered and random pores whose size ranges from a fraction of a nanometer to several nanometers. This discrete model can be used to analyze reactivity data at low temperatures where the reactions occur primarily on the surface of submicro- and micropores.

Modeling the Pore Structure of Biochars

The importance of biochar

Biochar is charcoal generated for intentional soil amendment by pyrolyzing sustainable biomass feedstocks. Pyrolysis converts biomass into a material with 70–80% carbon, which is about 30–40% of the original carbon in the biomass.[38] Biochars have high carbon sequestration value because a significant fraction of their carbon content resists microbial or chemical degradation and can stay in the ground for hundreds or thousands of years.[39] A recent study by Molina et al.[40] placed carbon sequestration by biochar high on the list of strategies for reducing carbon emissions, because it can be deployed rapidly and relatively cheaply. Woolf et al.[41] estimated that global deployment of biochar has the potential to sequester up to 1.8 Gt of carbon per year and up to 130 Gt over a century. Thus, biochar can mitigate a significant fraction of the 15 Gt/year of total global anthropogenic emissions.[41]

At the same time, properly "engineered" charcoals can increase the water holding and cation exchange capacities of soils, improving the ability of plants to survive under drought conditions and reducing fertilizer runoff into watersheds.[42] The environmental performance of biochars depends on their ability to absorb, retain, and release water and nutrients. These biochar properties are controlled by their pore structure and surface chemistry, which can vary widely depending on the composition of the biomass feedstocks and the pyrolysis conditions employed during biochar production.

The micropore structure of biochars

Nitrogen adsorption measurements revealed that biochars produced in our laboratory were very microporous with the vast majority of their pores being smaller than 2 nm.[38] Moreover, the hysteresis observed in the adsorption/desorption isotherms indicated the presence of narrow, slit-like pores.[43] These observations are consistent with a molecular structure of biochars that consists of a mix of (a) aromatic carbon in an amorphous mass and (b) nanometer-size crystallites composed of graphitic-like layers of aromatic carbon clusters that are arranged turbostratically.[44–46] These structures have been confirmed with nuclear magnetic resonance (NMR)[38] and X-ray diffraction (XRD) measurements.[46] We can conclude that the micropores of biochars consist of two subpopulations: randomly distributed pores and domains of orderly arranged pores. Random pores are formed between the domains of amorphous carbon, whereas the ordered pores are the slits formed between the graphitic-like layers of the crystalline phase.

Thermogravimetric experiments and data analysis

For a typical thermogravimetric experiment, a small amount of biochar is loaded on the sample of the sensitive microbalance of a thermogravimetric analyzer (TGA).[38] After removing the moisture, the sample is heated to the final reaction temperature in an inert atmosphere. When the desired temperature is reached, the carrier gas is switched from inert to air and combustion proceeds to completion. The biochar reactivity $R(t)$ can be computed from the sample weight using the formula

$$R(t)=\frac{dx}{dt}=-\frac{1}{m_0-m_f}\frac{dm(t)}{dt} \tag{1}$$

where x is the conversion of the combustion reaction defined by

$$x=\frac{m_0-m(t)}{m_0-m_f} \tag{2}$$

and where $m(t)$ is the measured weight of the sample at time t, m_0 is the initial weight of the sample, and m_f is the final weight of the sample (ash).

Let $S_g(x)$ be the total pore surface area that varies with conversion as pores grow and coalesce. The reaction rate $R(x)$ can then be expressed by

$$R(x)=a\cdot S_g\cdot f\left(c_f,T\right) \tag{3}$$

where a is a surface activity factor $(0<a<1)$ to account for the fact that reaction occurs only on a fraction of the total pore surface area $S_g(x)$, T and c are the reaction temperature and oxygen concentration, respectively, and $f\left(c_f,T\right)$ is a function that describes the kinetics of the reaction. We can isolate the surface area evolution pattern, however, if we normalize $R(x)$ by the reaction rate at some low conversion x_0

$$R^*(x)=\frac{R(x)}{R(x_0)}=\frac{S_g(x)}{S_g(x_0)} \tag{4}$$

We set the reference conversion to $x_0=0.1$ to minimize uncertainties in the computation of the initial reaction rate caused, for example, by the small temperature excursions that are common artifacts of the controllers of TGA equipment.

Development of a discrete pore structure model

The first step of our approach is to generate a nanoscale model of the pore structure of highly heterogeneous solids on a 3-D computational grid with cubic computational elements (or voxels). We should note here that the current model is a significant generalization of the algorithm we presented in an earlier study that used 2-D simulations to describe the controlled release of bioactive agents from multicomponent bioerodible devices.[47]

Domains of two solid components are distributed on the grid to simulate reactants that may have different specific reactivities and dispersions. Slit pores of fixed thickness are distributed in one of the solid components that will be denoted as the "crystalline" phase from now on. Finally, cylindrical overlapping pores are randomly distributed in the solid matrix. The diameters of the random pores follow a normal distribution whose mean is significantly larger than the thickness of the slit pores. The total volumes and size distributions of the ordered and random pore subpopulations are adjusted to match the experimentally determined micro- and mesoporosities, as well as any available information about the shape of the pores or the size of amorphous and crystalline domains in the case of biochars. Figure 1 shows a typical cross section of the 3-D arrays used for our simulations.

The generated porous solids are then eroded using rules that simulate a gas-solid, noncatalytic reaction that takes place in the kinetic control regime. If $V_i, i=1,2$ is the volume of phase i, the reaction rate r_i of that phase can be written as

$$r_i=\frac{dV_i}{dt}=\left(\frac{MW_i}{\rho_i}\right)\cdot S_i\cdot f\left(c_f,T\right) \tag{5}$$

where S_i is the total area of phase i exposed to the gaseous reactant, ρ_i and MW_i are the density and molecular weight of the solid phase, and $f\left(c_f,T\right)$ is the rate expression of the chemical reaction that is constant for a given concentration c_f of the gaseous reactant and reaction temperature T. Equation 5 then yields

$$r_i=\gamma_i S_i \qquad \text{with} \qquad \gamma_i=\left(\frac{MW_i}{\rho_i}\right)\cdot f\left(c_f,T\right) \tag{6}$$

where γ_i is the constant intrinsic reaction rate for given c_f and T.

Let us assume that the initial grid has N_0 cubic computational cells with each cell having a side equal to L and volume $V_0=L^3$. Let us also assume that $N_{1,0}$ computational cells contain solid component 1 (i.e., they belong to the crystalline phase), $N_{2,0}$ cells contain component 2 (i.e., they belong to the amorphous phase). The total porosity of our solid is then given by

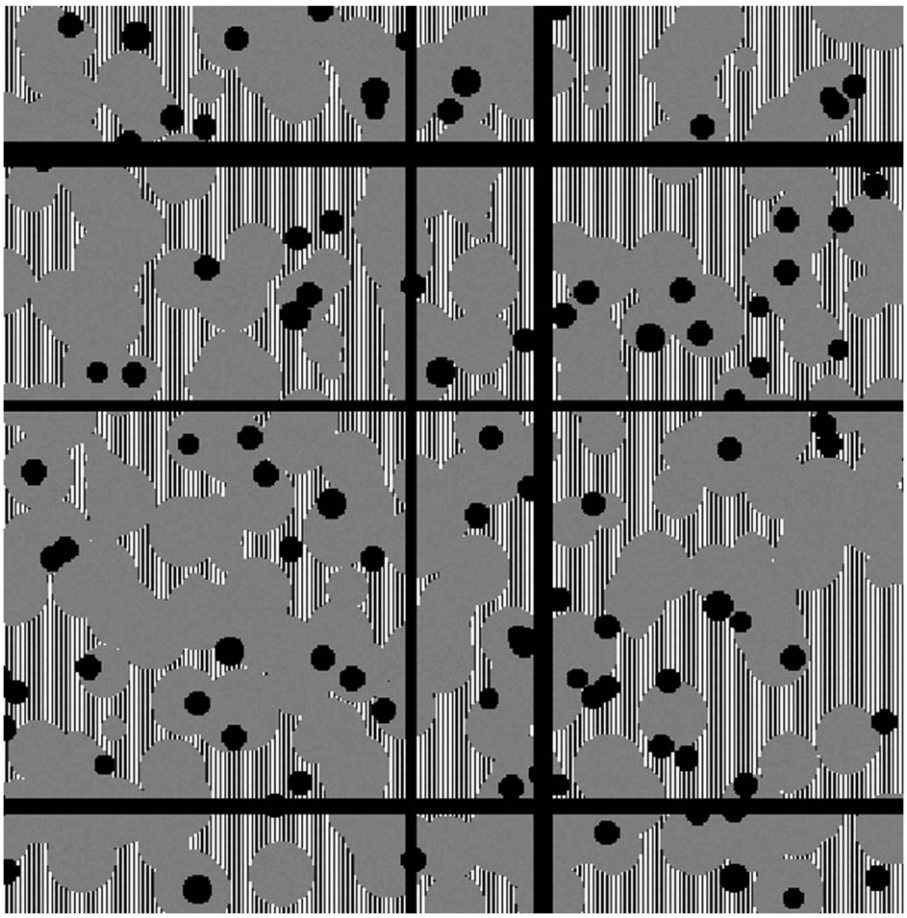

Figure 1. Cross section of the initial configuration of the nanoscale model for a porous solid.

Crystalline phase domains consist of thin layers of aromatic clusters (white straight lines) separated by slit pores (gray straight lines), while the amorphous phase is formed by overlapping spherical domains (gray areas). Cylindrical pores (black areas) provide the avenues for the gaseous reactant to reach the particle interior. For a typical simulation, the length of the side of the cross-section is 200 nm; the slit pores are 0.5 nm in size and the average radius of the cylindrical pores is 5 nm.

$$\varepsilon_t = \frac{N_0 - N_{10} - N_{20}}{N_0} \tag{7}$$

As the two solid reactants are consumed, the volume of solid present in every computational cell is updated in an iterative fashion. Each iteration corresponds to a different time level $t_0, t_1, t_2, ..., t_k, ...$ where $t_{k+1} = t_k + \Delta t$. To simplify the definition of normalized variables, we define Δt as the time required to consume a layer with thickness L of the solid reactant with the smaller intrinsic reaction rate. We also define the normalized time θ as $\theta = t/\Delta t$.

The reaction algorithm can then be written as follows

For the k-th time step $(k = 1, 2, ..., M)$

1. For every computational cell $j = 1, 2, ..., N$, determine first if it contains any solid.
2. If it does, determine if any of its faces are exposed to reactant.
3. If at least one face is exposed to reactant, compute the volume fraction $(\Delta V_j)^k$ that will react during the k-th time step as follows

$$(\Delta V_j)^k = \begin{cases} \gamma_1 \cdot S_j \cdot \Delta t & \text{if cell } j \text{ belongs to phase 1} \\ \gamma_2 \cdot S_j \cdot \Delta t & \text{if cell } j \text{ belongs to phase 2} \end{cases} \tag{8}$$

where γ_1 and γ_2 are the intrinsic rates for the crystalline and amorphous phases, respectively, and S_j is the surface area of the computational cell that is exposed to reactant and Δt is the time step.

4. Once all computational cells have been updated, the conversion χ^k and reaction rate r^k of the combined solid at time $t = k \cdot \Delta t$ are calculated as follows

$$\chi^k = \chi^{k-1} + \frac{\sum_{j=1}^{N} (\Delta V_j)^k}{N_0 V_0} \tag{9}$$

$$r^k = \frac{\sum_{j=1}^{N} (\Delta V_j)^k}{N_0 V_0 \cdot \Delta t} \tag{10}$$

We also compute the conversions and reaction rates for the crystalline and amorphous phases using Eqs. 9 and 10 but summing only over the computational cells that belong to the appropriate phase.

5. Steps 1 through 4 are repeated until both solid phases are completely reacted.

To facilitate comparisons with experimental data, the reaction rates are usually presented as functions of conversion χ and the normalized reaction rates are computed using as reference value the rate at 10% conversion

$$r^*(\chi)=\frac{r(\chi)}{r(\chi_0)} \tag{11}$$

If the intrinsic reactivities of the two solid components are equal, it is easy to see from Eqs. 6 and 10 that the normalized reaction rate $r^*(\chi)$ gives the evolution pattern of the total pore surface area of the solid and can be directly compared to the experimental normalized rate computed by Eq. 4. When the two components have unequal reactivities, the normalized rate $r^*(\chi)$becomes a linear combination of the evolution patterns of the reacting surface areas of the two components. In either case, $r^*(\chi)$is a "fingerprint" reactivity pattern that can be used to characterize the pore structure of a reactant by comparing model predictions to thermogravimetric reactivity data.

To smooth out the noise that is inherent in discrete simulation data, we also compute the least-squares approximations $\hat{\chi}(t)$ and $\hat{\chi}_i(t)$, $i=1,2$ to the conversions of the total solid χ and the individual components $\chi_i, i=1,2$ These computations are performed using piecewise B-splines.[48] The reaction rates for the individual phases and the overall solid $\hat{r}_1(t)$, $\hat{r}_2(t)$ and $\hat{r}(t)$ are then computed by differentiating the least-squares approximations to the conversions.

Results and Discussion

We carried out a systematic parametric study to demonstrate how key structural parameters affect the reactivity patterns. To create nanostructures that can accurately simulate the reaction of biochars, we randomly distributed on a 400 $\times$ 400 $\times$ 400 computational grid domains of crystalline and amorphous solids. The amorphous domains consisted of overlapping spheres whose diameter followed a normal distribution with user specified mean and standard deviation. Crystalline phase filled the space between the amorphous domains. Each crystalline domain consisted of thin, parallel layers of solid separated by slit pores, which represented the submicropores detected in biochars.[38] Finally, we randomly scattered on the grid cylindrical pores with specified cross-sectional shapes and size distributions to match the experimentally measured micropore properties of biochars.[38] The larger random pores penetrated the 3-D grid in all directions to allow the gaseous reactant to penetrate the nanopore structure.

The generation of the initial nanopore structures is a stochastic process and, thus, every simulation run will produce different results. To assess the variability of our model predictions, we generated 10 initial realizations of the micropore structure with the same values of the pore structural parameters (e.g., solid volume in each phase, phase domain size distribution, submicropore and micropore volume, micropore-size distribution, etc.). These realizations were then reacted to compute the average reactivity patterns. The coefficient of variation for the computed conversion values never exceeded 2% at all time levels and was typically around 0.5%. In addition, we performed a limited set of simulations using 800 $\times$ 800 $\times$ 800 computational grids. Results from runs with the larger grid were within the variability estimated from simulations performed on the smaller grid for the same structural parameters. Simulations on 400 $\times$ 400 $\times$ 400 grids required from 40 to 370 min of computational (CPU) time on a Macintosh workstation with dual quad-core 2.93-GHz Xeon processors.

To account for diffusional resistance in the submicropores, we assumed that the slit pores present in the crystalline domains are initially filled with a fictitious reacting phase. When there are no diffusional limitations in the slit pores, we set the intrinsic reactivity of the fictitious phase filling the slit pore to a much higher value than that of the crystalline solid phase. When the gaseous reactant reaches a slit pore, the fictitious phase reacts rapidly allowing the gaseous reactant to fully penetrate all parts of the slit pore that were previously inaccessible to the reactant. After that point, reaction occurs on all the exposed surfaces of the slit pore.

To simulate strong diffusional limitations, on the other hand, we set the intrinsic reactivity of the fictitious solid to be equal to the intrinsic reactivity of the crystalline solid. When the gaseous reactant reaches a slit pore that is still filled with the fictitious phase, it cannot penetrate into the pore interior because the "filler" phase recedes at the same rate as the pore walls. Thus, reaction occurs only on the mouths of the slit pores where they open into the larger random micropores.

Differential pore diffusion limitations strongly affect the reactivity patterns

Figure 2 presents the conversion χ vs. normalized time θ for the total solid as well as the crystalline and amorphous phases. For this run, both solid phases are assumed to have equal intrinsic reactivities $(\gamma_1=\gamma_2)$. Equation 6 then implies that the reaction rates of the two solid phases will be proportional to the magnitude of the surface area of each phase that is exposed to the gaseous reactant. As Figure 2 shows that the crystalline phase reacts much faster than the amorphous phase, we can immediately conclude that the pore structures and, consequently, the reacting surface areas of the two phases evolve at rates that are dramatically different. For this run, there are no diffusional limitations in the small slit pores of the crystalline phase. Thus, whenever the gaseous reactant reaches the mouth of a slit pore, it will penetrate rapidly into the slit to react on the entire surface area of the pore walls. The walls of the slit pores are very thin as

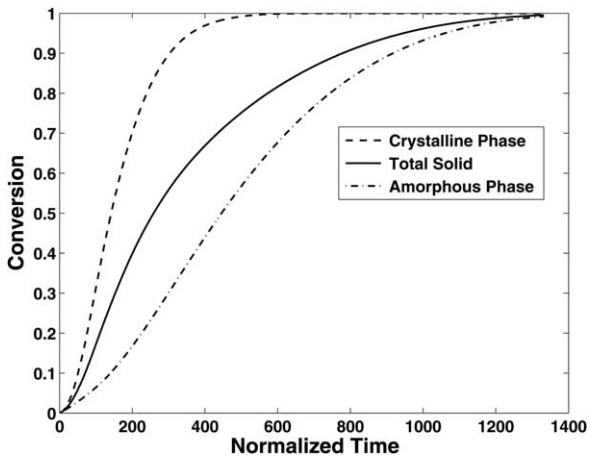

Figure 2. Crystalline phase reacts faster than the amorphous phase, even though both solids have the same intrinsic reactivity.

There are no diffusional limitations in the slit pores for this run. Data: ratio of phase volumes V_1/V_2 = 1.4—Dispersion parameter of amorphous phase δ_2=0.075—Porosity due to random cylindrical pores ε_r=0.15—Average radius of random pores r_p = 5 nm.

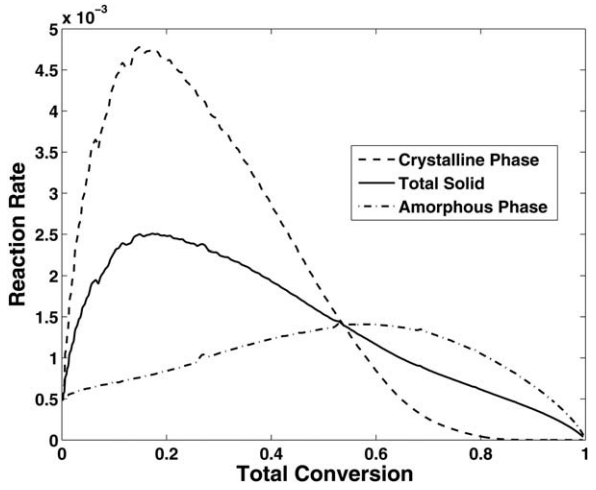

Figure 3. Reaction rates vs. total conversion for the crystalline phase, amorphous phase, and total solid.

There are no diffusional limitations in the slit pores for this run. All other parameter values are the same as in Figure 2.

they are formed by graphitic-like sheets of aromatic carbon clusters.[38,44,46] As a result, reacting pore walls will disappear quickly and the reactivity patterns will exhibit sharp peaks at low overall conversions.

Figure 3 presents the rates r_1, r_2, and r vs. the total solid conversion χ. Again, this figure uses the raw simulation data to demonstrate the low level of noise introduced by the discrete simulation algorithm. Figure 3 shows that the reaction rate for the crystalline phase reaches its maximum when about 15% of the total solid has reacted, whereas the rate for the amorphous phase exhibits a much slower rise reaching a less pronounced peak at about 50% conversion. Clearly, the overall reactivity pattern is determined by a superposition of the reactivity patterns of the individual phases with a maximum around 15% conversion and a gradual decrease after the maximum due to the still rising rate of the amorphous peak that does not peak until 50% of the total solid has

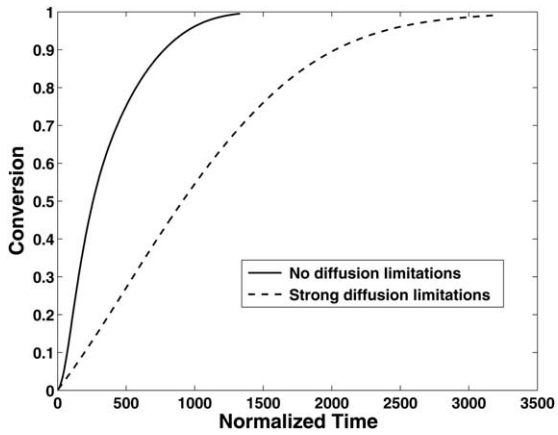

Figure 4. Strong diffusional limitations in the slit pores significantly increase the time required for complete conversion.

All pore structure parameters for these two runs are the same as in Figure 2.

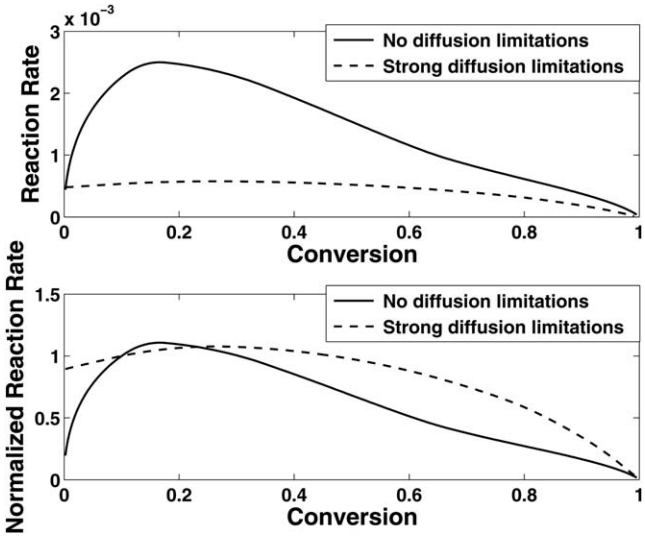

Figure 5. Strong diffusional limitations in the slit pores not only slow down the overall reaction rate of the solid (top panel), but they drastically change the reactivity pattern expressed by the normalized overall reaction rate (bottom panel).

All pore structure parameters for these two runs are the same as in Figure 2.

reacted. This also explains how inflection points appear on the reactivity patterns.

The appearance of diffusional limitations in the small slit pores completely changes the reactivity patterns. As expected, strong diffusional limitations slow down the overall reaction (Figure 4 and top panel of Figure 5) and double the time required for complete conversion (Figure 4). Even more striking, however, is the effect of diffusional limitations on the reactivity pattern. When the gaseous reactant cannot penetrate the small slit pores, the normalized reaction rate exhibits a much flatter initial rise and a maximum in the 30–40% conversion range (bottom panel of Figure 5).

The effects of other pore structure parameters

Several other structural parameters can modulate the reactivity patterns. If we keep the intrinsic reactivities of the two phases equal $\left(\gamma_2/\gamma_1=1\right)$, a change of the phase volume ratio from $V_2/V_1=1.4$ to $V_2/V_1=3.0$ will slow down the overall reaction rate. This is because our model assumes that a reduction of the crystalline fraction will lead to a decrease of the overall porosity of the biochar. However, normalization of the reaction rates with respect to the rate at 10% total conversion brings the reactivity patterns much closer together. As shown by the corresponding curves of Figure 6, the significant change of the volume ratio from 1.4 to 3 (and the resulting decrease in total porosity by 20%) will have only a small effect on the reactivity patterns. When the phase intrinsic reactivities are unequal $\left(\gamma_2/\gamma_1=2\right)$, the same change in the phase volume ratio triggers a more pronounced effect as shown by the dotted curves of Figure 6.

Even though normalization of the reaction rates may partially suppress the effect of structural parameters, it is essential for correctly interpreting the experimental reactivity patterns obtained with thermogravimetric measurements.

As we have shown in earlier publications,[14,38] thermogravimetric analyzers may go through temperature "excursions" during the very early stages of the reaction due to the well-known oscillatory response of proportional-integral-derivative (PID) feedback controllers to disturbances caused by the start of an exothermic reaction. Thus, normalization is necessary to avoid uncertainties caused by rate fluctuations during the initial stage of the reaction.

The phase dispersion is another parameter that influences the reactivity patterns. Our model assumes that the amorphous phase consists of overlapping spherical domains whose radius follows a normal distribution with known mean and standard deviation (see Figure 1). The parameter δ_2 that quantifies the dispersion of the amorphous phase is the ratio of the average radius of the spherical amorphous domains over the characteristic length of the computational grid, which is taken to be equal to the length of its side. As shown in Figure 7, larger values of the phase dispersion parameter shift the maxima of the reactivity patterns to smaller conversions. An analysis of the simulation results shows that as δ_2 increases, the ratio of the external area of the amorphous domain clusters over their volume decreases. This lowers the maximum of the reaction rate of the amorphous phase and shifts it to higher conversions.

Model predictions and experimental TGA data

The discrete model provided very accurate approximations to thermogravimetric data for biochar combustion at low temperatures. We will only show here the results for an apple wood biochar whose reactivity patterns could not be fit with any of the available random pore or random grain models.

As we reported in an earlier study,[38] these apple wood biochars are very microporous. Their adsorption isotherms exhibit hysteresis that indicates the presence of narrow, slit-like pores. Brunauer-Emmett-Teller (BET) and Dubinin–Raduskevich analysis of adsorption data show micropore volumes as high as 0.15 cm^3/g and surface areas that can exceed 300 m^2/g under some production conditions. Moreover, NMR measurements indicate the presence of aromatic domains consisting of large clusters with 15–20 aromatic carbon atoms. All these observations are consistent with a molecular structure of biochars that consists of a mix of amorphous domains and crystallites with slit pores.

Using the available data, we generated structures consisting of crystalline and amorphous phases and reacted them to simulate combustion of these chars at low temperatures. Because it was not possible to independently measure the intrinsic reaction rates of the two phases, we assumed that both phases have the same specific reactivity. We assumed that the distance between the planes that define the slit pores was 0.5 nm, a value that is only slightly larger than the distance between planes of the graphite. The volume ratio of the amorphous and crystalline phases, the average radius of the cylindrical pores and its standard deviation, and the size of the amorphous domains were the adjustable parameters for this apple wood biochar. Reactivity patterns computed from experimental data and model predictions were normalized with respect to the reaction rate at 10% conversion.

Panel A of Figure 8 shows that the good agreement obtained between model predictions and TGA experiments for combustion of apple wood biochar in air at 350°C. For this run, we assumed that there were no diffusional limitations in the slit pores. The simulation results were able to accurately match the experimental reactivity pattern that exhibited a sharp maximum at low conversions.

When the combustion temperature was raised to 400°C, the experimental reactivity pattern of the same apple wood biochar shifted to higher conversion (Panel B of Figure 8). This shift indicates the appearance of diffusional limitations in the slit pores at the higher reaction temperature. By reducing the accessibility of the slit pores to the gaseous reactant, the model was again able to accurately fit the experimental reactivity pattern. All pore structural parameters were the same for the simulation runs of Panels A and B of Figure 8.

Similar agreement was observed between model predictions and experimental data for the combustion of corn stover biochars with oxygen at low temperatures.

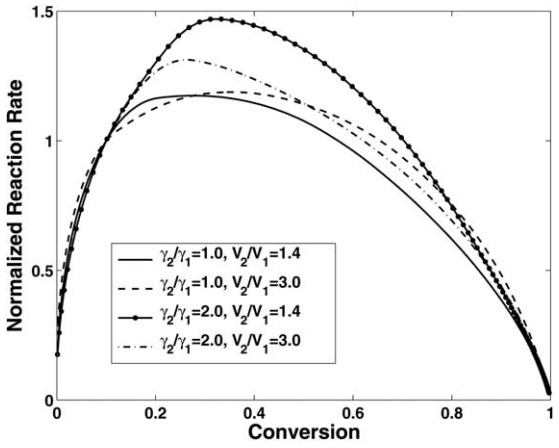

Figure 6. Reactivity patterns are strongly affected by changes in the intrinsic reactivity rates and the volume ratio of the two phases.

There are no diffusional limitations in the slit pores for these four runs. Data: dispersion parameter of amorphous phase $\delta_2=0.025$—Porosity due to random cylindrical pores $\varepsilon_r=0.15$—Average radius of random pores r_p = nm.

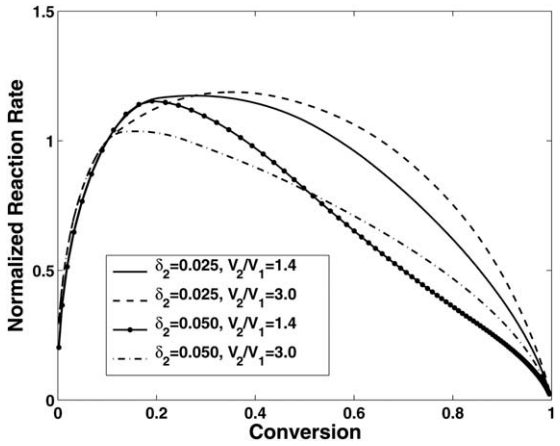

Figure 7. Reactivity patterns are also affected by the size of the spherical amorphous domains.

There are no diffusional limitations in the slit pores for these four runs. Data: phases have equal intrinsic reaction rates $(\gamma_1=\gamma_2)$—Porosity due to random cylindrical pores $\varepsilon_r=0.15$—Average radius of random pores $r_p=5$ nm.

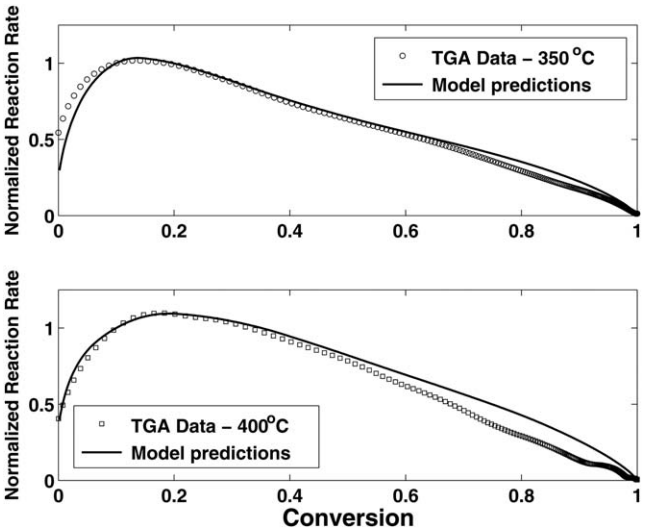

Figure 8. Model predictions agree well with TGA data for combustion of apple wood biochar at 350°C (top panel) and 400°C (bottom panel).

Data: volume ratio of the amorphous over the crystalline phase = 1.4—Spherical amorphous domains with dispersion parameter $\delta_2 = 0.09$—Both phases have the same specific reactivity.

Concluding Remarks

The nanoscale model described in this study cannot be used to simulate the combustion of biochars at high temperatures where strong diffusional limitations appear in meso- and macropores. Because biochars have pores with sizes ranging from 0.5 nm to more than 10 microns, the "brute force" approach used here would require computational grids with more than 10^{16} nonporous cells. To overcome this limitation, we use porous computational cells to generate "microscale" models that describe the macropore structure of biochars. Reaction now occurs primarily in the interior of the computational cells and follows the reactivity patterns that we have computed *a priori* with nanoscale models.

The combination of structural models, TGA reactivity measurements and diffusion-reaction theory provides a powerful framework that can help us gain new insights into the pore structure of biochars. This novel approach complements nicely the analytical techniques that are currently used to measure some of the pore structure properties of these important carbonaceous materials. A detailed characterization of the pore structure and surface chemistry of biochars is an essential prerequisite for understanding the fundamental mechanisms that modulate the ability of biochar-amended soils to absorb a fertilizer and release it again in a controlled fashion. This will facilitate the development of optimally "engineered" biochars that can lead to increased crop yields while minimizing the leaching of fertilizer to rivers and lakes.

Literature Cited

1. Caram HS, Amundson NR. Diffusion and reaction in a stagnant boundary layer about a carbon particle. *Ind Eng Chem Fundam.* 1977;16(2):171–181.
2. Mon E, Amundson NR. Diffusion and reaction in a stagnant boundary layer about a carbon particle. 2. An extension. *Ind Eng Chem Fundam.* 1978;17(4):313–321.
3. Mon E, Amundson NR. Diffusion and reaction in a stagnant boundary layer about a carbon particle. 3. Stability. *Ind Eng Chem Fundam.* 1979;18(2):162–168.
4. Mon E, Amundson NR. Diffusion and reaction in a stagnant boundary layer about a carbon particle. 4. The dynamical behavior. *Ind Eng Chem Fundam.* 1980;19(3):243–250.
5. Sundaresan S, Amundson NR. Diffusion and reaction in a stagnant boundary layer about a carbon particle. 5. Pseudo-steady-state structure and parameter sensitivity. *Ind Eng Chem Fundam.* 1980;19(4): 344–351.
6. Sundaresan S, Amundson NR. Diffusion and reaction in a stagnant boundary layer about a carbon particle. 6. Effect of water vapor on the pseudo-steady-state structure. *Ind Eng Chem Fundam.* 1980; 19(4):351–357.
7. Kumpinsky E, Amundson NR. Diffusion and reaction in a stagnant boundary layer about a carbon particle. 8. Comparison of lumped and distributed chemical kinetics. *Ind Eng Chem Fundam.* 1983;22(1):62–71.
8. Kumpinsky E, Amundson NR. Diffusion and reaction in a stagnant boundary layer about a carbon particle. 8a. Effect of the carbon dioxide reduction reaction. *Ind Eng Chem Fundam.* 1984;23(1):34–37.
9. Gavalas GR. A random capillary model with application to char gasification at chemically controlled rates. *AIChE J.* 1980;26(4):577–585.
10. Gavalas GR, Wilks KA. Intraparticle mass transfer in coal pyrolysis. *AIChE J.* 1980;26(2):201–212.
11. Bhatia SK, Perlmutter DD. A random pore model for fluid-solid reactions: I. Isothermal, kinetic control. *AIChE J.* 1980;26(3):379–386.
12. Bhatia SK, Perlmutter DD. A random pore model for fluid-solid reactions: II. Diffusion and transport effects. *AIChE J.* 1981;27(2): 247–254.
13. Zygourakis K, Arri L, Amundson NR. Studies on the gasification of a single char particle. *Ind Eng Chem Fundam.* 1982;21(1):1–12.
14. Ballal G, Zygourakis K. Evolution of pore surface area during noncatalytic gas-solid reactions. 1. Model development. *Ind Eng Chem Res.* 1987;26(5):911–921.
15. Ballal G, Amundson NR, Zygourakis K. Pore structural effects in catalytic gasification of coal chars. *AIChE J.* 1988;34(3):426–434.
16. Ballal G, Zygourakis K. Evolution of pore surface area during noncatalytic gas-solid reactions. *2. Experimental results and model validation. Ind Eng Chem Res.* 1987;26(9):1787–1796.
17. Kantorovich II, Bar-Ziv E. Microstructural evolution of char under oxidation induced by uneven heating. *Combust Flame.* 1994;97:61–78.
18. Liu G, Benyon P, Benfell KE, Bryant GW, Tate AG, Boyd RK, Harris DJ, Wall, TF. The porous structure of bituminous coal chars and its influence on combustion and gasification under chemically controlled conditions. *Fuel.* 2000;79(6):617–626..
19. Sotirchos SV, Amundson NR. Diffusion and reaction in a char particle and in the surrounding gas phase. A continuous model. *Ind Eng Chem Fundam.* 1984;23(2):191–201.
20. Sotirchos SV, Amundson NR. Diffusion and reaction in a char particle and in the surrounding gas phase. Two limiting models. *Ind Eng Chem Fundam.* 1984;23(2):180–191.
21. Sotirchos SV, Amundson NR. Dynamic behaviour of a porous char particle burning in an oxygen-containing environment. Part I: Constant particle radius. *AIChE J.* 1984;30(4):537–549.
22. Sotirchos SV, Amundson NR. Dynamic behaviour of a porous char particle burning in an oxygen-containing environment. Part II: Transient analysis of a shrinking particle. *AIChE J.* 1984;30(4):549–556.
23. Sotirchos SV, Amundson NR. Diffusion and reaction in a char particle and in the surrounding gas phase. A continuous model. *Ind Eng Chem Fundam.* 1984;23(2):191–201.
24. Sotirchos SV, Burganos VN. Intraparticle diffusion and char combustion. *Chem Eng Sci.* 1986;41(6):1599–1609.
25. Gavalas G. Analysis of char combustion including the effect of pore enlargement. *Comb Sci Technol.* 1981;24:197–210.
26. Feng C, Stewart WE. Practical models for isothermal diffusion and flow of gases in porous solids. *Ind Eng Chem Fundam.* 1973;12: 143–147.
27. Sahimi M, Gavalas GR, Tsotsis TT. Statistical and continuum models of fluid-solid reactions in porous media. *Chem Eng Sci.* 1990;45:1443–1502.
28. Sotirchos SV. On a class of random pore and grain models for gas solid reactions. *Chem Eng Sci.* 1987;42(5):1262–1265.

29. Williams A, Backreedy R, Habib R, Jones JM, Pourkashanian M. Modelling coal combustion: the current position. *Fuel*. 2002;81:605–618.
30. Zygourakis K. Effect of pyrolysis conditions on the macropore structure of coal-derived chars. *Energy Fuels*. 1993;7(1):33–41.
31. Cai YW, Zygourakis K. A multiscale transient model for combustion of highly porous chars. *Ind Eng Chem Res*. 2003;42(12):2746–2755.
32. Sandmann CW, Zygourakis K. Evolution of pore structure during gas-solid reactions—discrete models. *Chem Eng Sci*. 1986;41(4):733–739.
33. Zygourakis K, Sandmann CW. Discrete structural models and their application to gas-solid reacting systems. *AIChE J*. 1988;34(12):2030–2040.
34. Audier M, Oberlin A, Oberlin M, Coulon M, Bonnetain L. Morphology and crystalline order in catalytic carbons. *Carbon*. 1981;19(3):217–224.
35. Monthioux M, Oberlin M, Oberlin A, Bourrat X, Boulet R. Heavy petroleum products: microtexture and ability to graphitize. *Carbon*. 1982;20(3):167–176.
36. Joseph D, Oberlin A. Oxidation of carbonaceous matter—II: x-ray diffraction and transmission electron microscopy. *Carbon*. 1983;21(6):565–571.
37. Brooks JD, Taylor GH. The formation of some graphitizing carbons. In: Walker PL, Thrower PA, editors. Chemistry and Physics of Carbon, Vol 4. New York, NY: Marcel Dekker, 1968:243.
38. Sun H, Hockaday WC, Masiello CA, Zygourakis K. Multiple controls on the chemical and physical structure of biochars. *Ind Eng Chem Res*. 2012;51(9):3587–3597.
39. Lehmann J, Gaunt J, Rondon M. Bio-char sequestration in terrestrial ecosystems: a review. *Mitig Adapt Strat Global Chang*. 2006;11(2):395–419.
40. Molina M, Zaelke D, Sarma KM, Andersen SO, Ramanathan V, Kaniaru D. Reducing abrupt climate change risk using the Montreal protocol and other regulatory actions to complement cuts in CO_2 emissions. *Proc Natl Acad Sci USA*. 2009;106(49):20616–20621.
41. Woolf D, Amonette JE, Street-Perrott FA, Lehmann J, Joseph S. Sustainable biochar to mitigate global climate change. *Nat Commun*. 2010;1(5):1–9.
42. Lehmann J. A handful of carbon. *Nature*. 2007;447(7141):143–144.
43. Sing KSW, Everett DH, Haul R, Moscou L, Pierotti RA, Rouquerol J, Siemieniewska T. Reporting physisorption data for gas/solid systems with special reference to the determination of surface area and porosity. *Pure Appl Chem*. 1985;57(4):603–619.
44. Bourke J, Manley-Harris M, Fushimi C, Dowaki K, Nunoura T, Antal MJ. Do All carbonized charcoals have the same chemical structure? 2. A model of the chemical structure of carbonized charcoal. *Ind Eng Chem Res*. 2007;46(18):5954–5967.
45. Keiluweit M, Nico PS, Johnson MG, Kleber M. Dynamic molecular structure of plant biomass-derived black carbon (biochar). *Environ Sci Technol*. 2010;44:1247–1253.
46. Kercher AK, Nagle DC. Microstructural evolution during charcoal carbonization by x-ray diffraction analysis. *Carbon*. 2003;41:15–27.
47. Zygourakis K, Markenscoff PA. Computer-aided design of bioerodible devices with optimal release characteristics: a cellular automata approach. *Biomaterials*. 1996;17(2):125–135.
48. de Boor C. A Practical Guide to Splines. New York, NY: Springer-Verlag, 1978.

Manuscript received Dec. 22, 2012, and revision received Apr. 10, 2013.